Available online at www.sciencedirect.com
SCIENCE DIRECT
Icarus 173 (2005) 349–361
ICARUS
www.elsevier.com/locate/icarus

Numerical experiments with rubble piles: equilibrium shapes and spins

Derek C. Richardson *, Pradeep Elankumaran, Robyn E. Sanderson

Department of Astronomy, Computer and Space Sciences Building, Stadium Drive, University of Maryland, College Park, MD 20740-2421, USA

Received 14 July 2004; revised 11 September 2004

Available online 6 November 2004

Abstract

We present numerical experiments investigating the shape and spin limits of self-gravitating "perfect" rubble piles that consist of identical, smooth, rigid, spherical particles with configurable normal coefficient of restitution and no sliding friction. Such constructs are currently employed in a variety of investigations, ranging from the formation of asteroid satellites to the dynamical properties of Saturn's densest rings. We find that, owing to cannonball stacking behavior, rubble piles can maintain non-spherical shapes without bulk spin, unlike a fluid, and can spin faster than a perfect fluid before shedding mass, consistent with the theory for the more general continuum rubble pile model (Holsapple, 2004, Icarus 172, 272–303). Rubble piles that reassemble following a catastrophic disruption reconfigure themselves to lie within stability limits predicted by the continuum theory. We also find that coarse configurations consisting of a small number of particles are more resistant to tidal disruption than fine configurations with many particles. Overall this study shows that idealized rubble piles behave qualitatively in a manner similar to certain granular materials, at least in the limit where global shape readjustments and/or mass shedding begins. The limits obtained here may provide constraints on the possible internal structure of some small Solar System bodies that have extreme shapes or are under high stress. Amalthea is presented as a case study.

Keywords: Asteroids; Planetesimals; Rotational dynamics; Solid body tides; Satellites of Jupiter

1. Introduction

1.1. Motivation

The possibility that many small bodies in the Solar System—from comets to asteroids to small moons—may be highly fractured, and thus have low tensile strength,[1] has received increased consideration based on growing, though largely circumstantial evidence (see Richardson et al., 2002, for a review). We define a "gravitational aggregate" to be a body of low tensile strength made up of competent pieces and bound together by gravity. We define a "rubble pile" to be a special case of gravitational aggregate with virtually *zero* tensile strength and moderate porosity (as might arise from jumbling of the component pieces) that may or may not represent the actual internal structure of some of these Solar System bodies. For the purpose of this paper, a "perfect" rubble pile has zero tensile strength and is made up of identical, smooth, rigid, spherical particles of uniform internal density that cannot interlock in any way and that cannot change shape. An appropriate analogy is a pile of billiard balls. Perfect rubble piles have the advantage that they are among the simplest granular materials to model numerically, since collisions between spheres are always central impacts at a single point of contact and the external gravitational potential due to a spherical mass distribution is equivalent to the potential due a single point located at the center of the distribution and having the same total mass.

* Corresponding author. Fax: +1-301-314-9067.
E-mail address: dcr@astro.umd.edu (D.C. Richardson).

[1] *Tensile strength* is the ability to resist stretching, such as that imparted by a tidal encounter. Distinct from this is *shear strength*, which is the ability to resist shearing or sliding motions. Loosely consolidated material generally has no tensile strength; but, when the particles are being forced together, it will have shear strength by virtue of geometric interlocking of its particles. It will not have shear strength in the absence of confining compressive pressure. For example, dry sand has shear strength when under compressive pressures, but no tensile strength; liquid water has neither shear nor tensile strength.

0019-1035/$ – see front matter
doi:10.1016/j.icarus.2004.09.007

A variety of investigations have been carried out that employ perfect rubble piles in their numerical models, including, most recently, tidal disruption of asteroids (Richardson et al., 1998; Richardson and Scheeres, 2002), planetesimal evolution (Leinhardt and Richardson, 2002; Tanga et al., 2004), ring particle dynamics (Porco et al., 2003; Walsh and Richardson, 2004), and comet splitting (Weissman et al., 2003). Alternative rubble pile models employ ellipsoidal (Roig et al., 2003) or polygonal (Korycansky, 2004) particles, but have not yet been employed in full-scale simulations. Other investigations have precluded direct modeling with perfect rubble piles due to the large number of particles involved (and instead simply merge particles together when they come back in contact), but will likely employ such techniques in the future as algorithms and hardware improve. Examples include the post-collision formation of asteroid families (Michel et al., 2004) and asteroid satellites (Durda et al., 2004). It is therefore important to understand how idealizations in the model may affect the outcomes so that proper inferences may be drawn.

It is also of intrinsic interest to study perfect rubble piles as a special limiting case of the general problem of self-gravitating granular media, a topic with a range of applicability, from theoretical mechanics to material transport on asteroid surfaces. In particular, recent interpretation of asteroid lightcurves (e.g., Pravec et al., 2002) shows that all asteroids with diameters in excess of 150 m are (within uncertainties) inside the limits for mass shedding at the equator for unconsolidated materials, as noted by Harris (1996). They are also within the more stringent equilibrium limits discussed here for rubble piles with no cohesion, using either the continuum results of Holsapple (2001) or the results of this paper. For the smaller bodies, the so-called "fast rotators," much larger spins are observed from the lightcurves; but, as noted by Pravec et al. (2002), very small cohesion could accommodate all observed spins. Indeed, Holsapple (2003) shows that explicit spin-limit curves for bodies with cohesion smoothly bound all the data if the body has a cohesion of only a few kPa, which is on the order of the cohesion of the lunar regolith.

In this paper, our first approach to investigating the properties of perfect rubble piles is to determine how they compare to perfect fluids and continuum granular materials by testing their spin and shape limits numerically. Since analytical descriptions of fluid behavior (as well as more general granular configurations; cf. Section 1.3) exist, this provides a good reference point for finding properties unique to rubble piles. We also briefly consider the equilibrium states of a perfect rubble pile under tidal stress.

In the remaining subsections of this introduction we present more definitions, outline previous work, and detail certain special cases that will prove useful in comparing our results with earlier work. In the remainder of the paper, we outline our numerical procedure in Section 2, present and discuss our results in Section 3, and offer our conclusions in Section 4.

1.2. Definitions

For the purpose of comparing our numerical models to continuum models (i.e., those containing effectively an infinite number of particles), we restrict our discussion to *triaxial ellipsoids* of uniform mass density,[2] that is, bodies whose surfaces satisfy the equation

$$\frac{(x-x_c)^2}{a_1^2}+\frac{(y-y_c)^2}{a_2^2}+\frac{(z-z_c)^2}{a_3^2}=1, \tag{1}$$

where (x_c, y_c, z_c) is the location of the body center (coincident with the center of gravity), (x, y, z) is a point on the surface measured in the body frame (i.e., the frame in which the x, y, and z directions are aligned with the major, intermediate, and minor axes of the body, respectively), and a_1, a_2, and a_3 are the semi-major, semi-intermediate, and semi-minor axis lengths of the ellipsoid, respectively (so $a_1 \geqslant a_2 \geqslant a_3$).

We define the axis ratios $q_2 \equiv a_2/a_1$ and $q_3 \equiv a_3/a_1$, so that $q_3 \leqslant q_2 \leqslant 1$. With these definitions, a perfect sphere has $q_3 = q_2 = 1$, an oblate ellipsoid (which we will call an *obloid*, shaped like a soy burger) has $q_3 < q_2 = 1$, and a prolate ellipsoid (which we will call a *proloid*, shaped like a tofu dog) has $q_3 = q_2 < 1$. Obloids and proloids by this definition are *biaxial* ellipsoids, i.e., degenerate examples of triaxial ellipsoids. Obloids are sometimes called *spheroids*, hence the term "Maclaurin spheroid."

1.3. Previous work

Holsapple (2001) provides a concise review of the development of spin/shape equilibrium theory for fluids and solids over the past three-and-a-half centuries. This review will not be repeated here, apart from noting that for perfect, self-gravitating, incompressible fluids, there is a limited locus of stable permissible spin and shape combinations, of which the Maclaurin spheroids and Jacobi ellipsoids are the most familiar examples (also see Binney and Tremaine, 1987, Section 4.6.1). Figure 2a (cf. Section 3) shows the Maclaurin and Jacobi curves together on a plot of normalized body spin vs. axis ratios q_2 (red curve) and q_3 (green curve). These are numerical solutions to Eq. (4-197) of Binney and Tremaine (1987) obtained using the GNU Scientific Library.[3] The curves indicate permissible q_2 and q_3 values for a fluid, where the upper segment of both curves together describe the Maclaurin spheroids (q_2 is fixed at 1 and only q_3 varies with spin, so these are obloids) and the lower segments describe the Jacobi ellipsoids (for which there is a unique q_2, q_3 pairing for each allowed spin).

[2] Note that a rubble pile does *not* strictly have uniform mass density, since it consists of solid spheres interspersed with empty space, but over volumes large compared to the component spheres the bulk density is the same everywhere in the body.

[3] http://www.gnu.org/software/gsl/.

The unstable extension of the Maclaurin sequence is not shown.

In his paper, Holsapple (2001)[4] developed a detailed theory of the possible spin and shape configurations of solid cohesionless bodies as a function of the Mohr–Coulomb friction angle ϕ of the component material in the continuum limit. (A perfect fluid has $\phi = 0°$; typical terrestrial granular materials have $\phi \sim 30°$.) In common experience, grains of sand poured onto a table will form a pile with a maximum slope, or angle of repose, equal to the angle of friction, namely $\sim 30°$, while water poured onto a table will not form a pile at all. For sand, a combination of interparticle friction, cannonball stacking, and geometric locking keeps the pile from spreading out. In other words, sand has shear strength in some conditions. Interestingly, adding *some* water to a sand pile allows $\phi \to 90°$ or more, which is why sandcastles can stand up (Hornbaker et al., 1997; also Albert et al., 1997). Holsapple (2001) found that, unlike perfect fluids, cohesionless bodies can occupy a *region* of permissible shape and spin combinations, roughly centered on the classic fluid curves. Comparing his results against a database of 845 real asteroids, Holsapple (2001) showed that virtually all asteroids are consistent with cohesionless moderate-porosity structures in the granular continuum limit.[5] However, the continuum models and the perfect rubble pile models here are different, since the latter consist of finite-size components that are not in the continuum limit. Therefore, an important justification for the present study was to investigate the differences.[6] Indeed, we find that the Holsapple (2001) $\phi = 40°$ limiting curves for proloids are a good representation of our numerical results (cf. Section 3).

Using a different approach, Washabaugh and Scheeres (2002) investigated the energy and stress distributions in spinning elastic ellipsoids using a constitutive law, with total mass and angular momentum strictly conserved. In this approach, for a given angular momentum, incompressible bodies in the minimum elastic energy state correspond to Maclaurin spheroids and Jacobi ellipsoids, but do not match well with observations of asteroids. Moreover, if asteroids are incompressible rubble piles, Washabaugh and Scheeres (2002) showed they would be under tensile stress and so require some type of cohesion between the component material. On the other hand, if some compressibility is allowed, the elastic energy minima are broader and can encompass observations. They conclude that rubble piles could be consistent with observations.

[4] Also see Holsapple (2004) for new, completely generalized closed-form derivations, viz. his Eq. (6.3).

[5] See Farinella et al. (1981) and Weidenschilling (1981) for earlier studies of fluid spin/shape equilibria among asteroids.

[6] Preliminary comparisons were performed and reported by Bottke et al. (1999), who found broad similarities between rubble piles and sandpiles in 2D, including a rough match for an empirically derived angle of repose.

1.4. Special cases of the continuum theories

It is instructive to consider a few special cases in the continuum limit as fiducials for our numerical experiments. The Maclaurin and Jacobi curves have already been mentioned (cf. Fig. 2a). Since our perfect rubble piles consist of finite solid components, the spin limit of a test particle to remain on the surface of a solid body is also of interest. This can be obtained simply by equating the centrifugal acceleration of the test particle due to rotation of the body to the gravitational acceleration of the particle from the body. For the case of a rigid sphere, the spin limit at the equator can be expressed as

$$\frac{\omega_{\max}}{\sqrt{2\pi G\rho}} = \sqrt{\frac{2}{3}} \doteq 0.82, \tag{2}$$

where ρ is the bulk density of the body. For a rigid proloid, it is necessary to perform a volume integral over the mass density to compute the gravitational acceleration (Appendix A; also see Harris, 2002, Appendix). The result for a particle on the tip is

$$\frac{\omega_{\max}}{\sqrt{2\pi G\rho}} = \frac{1}{e^{3/2}}\sqrt{(e^2-1)\left[2e + \ln\left(\frac{1-e}{1+e}\right)\right]}, \tag{3}$$

where $e \equiv \sqrt{1-q_2^2}$ is the eccentricity of the body. A similar expression can be derived for a particle on the equator of an obloid. Note Eq. (3) is equivalent to the cohesionless proloid granular pile case in the limit of 90° friction angle (cf. the $\phi = 90°$ curve in Fig. 3 of Holsapple, 2001).

Often the ellipsoid is approximated as a point mass for the purpose of computing the gravitational acceleration, leading to the following approximate spin limit for a rigid proloid (see, e.g., Harris, 1996; also Pravec and Harris, 2000):

$$\frac{\omega_{\max}}{\sqrt{2\pi G\rho}} = \sqrt{\frac{2(1-e^2)}{3}}. \tag{4}$$

Equations (3) and (4) are plotted in Fig. 2a (cf. Section 3), the former as a dashed blue curve, the latter as a dotted magenta line. Note that both curves have the expected limiting behavior in the sense that they are coincident at the origin and at the limit of the spherical case given by Eq. (2).

Also shown among the fiducials of Fig. 2a is the case, for a proloid, of granular material with $\phi = 40°$, from Fig. 3 of Holsapple (2001). The lower and upper limit curves, shown as dotted and dashed light gray lines, respectively, delineate the region inside which a cohesionless granular pile with $\phi = 40°$ is within yield (that is, material in the pile does not start to flow). We will find that all the rubble pile cases studied here lie between these fiducials.

2. Method

All simulations were carried out using `pkdgrav`, an N-body gravity tree code that allows for interparticle col-

lisions (Richardson et al., 2000; Stadel, 2001). Initial conditions were generated and analysis was performed using codes auxiliary to `pkdgrav`. Perl scripts were written to automate the generation and analysis of the hundreds of runs performed. The runs themselves were managed using the `condor` high-throughput environment[7] on a private cluster of PCs in the Department of Astronomy at the University of Maryland.[8] Typically a run required ~ 8 CPU h or less to complete.

2.1. Initial conditions

The initial conditions for each run consisted of a single rubble pile rotating uniformly about the axis of maximum inertia (equivalently, the shortest axis). In order to investigate the effect of numerical resolution on the outcome, rubble piles with $N \sim 100$ and $N \sim 1000$ particles were generated. In each case, the desired axis lengths were specified (only proloids were considered as initial conditions for this investigation, so $a_2 = a_3$ for each body at the start) and the resulting ellipsoidal volume was filled with equal-size spheres in a hexagonal close-packed (HCP) configuration (Richardson et al., 1998). Note that since the component spheres in HCP configurations are identical, it was generally not possible to fill the target shapes with exactly the desired number of particles (e.g., for a spherical shape with a target $N = 1000$, the closest matching configuration with $N \leqslant 1000$ has $N = 955$; for non-spherical shapes the component particle radius was adjusted to stay as close to the desired N as possible; see Section 2.3.1 for other caveats regarding the shapes of rubble piles). Starting axis ratios q_2 of $0.1, 0.2, \ldots, 1$ were investigated (recall $q_3 = q_2 < 1$ for proloids). The desired spin was imposed by setting the velocity of each sphere according to $\mathbf{v}_i = \boldsymbol{\omega} \times \mathbf{r}_i$, where $\boldsymbol{\omega}$ is the (unnormalized) spin vector and $\mathbf{r}_i$ is the position vector (x_i, y_i, z_i) of each sphere relative to the body center of mass. Starting spins of $0.02, 0.04, \ldots, 0.84$ (in units of $\sqrt{2\pi G\rho}$) were tested. The starting bulk density ρ was set to 2000 kg m^{-3} (to represent a generic asteroid density, but the results are scaled by density anyway) by varying the internal density of the N generated particles appropriately. Figure 1 shows a typical starting case.

For technical reasons, `pkdgrav` does not allow particles to be in contact initially, so the rubble pile particles were reduced in radius by 1% at the start. Past experience has shown that such a small perturbation has negligible effect on the outcome and that it is not necessary to first equilibrate each rubble pile, such as by allowing the velocity dispersion to reach a constant value, before using it in a simulation.

2.2. Simulations

Each simulation used a timestep of ~ 5 s ($\lesssim 0.1\%$ of the "dynamical time" $\sim 3/\sqrt{G\rho}$ for a single particle; note that ρ for a particle is typically 1.5–2 times larger than ρ for the rubble pile due to the macroporosity). Runs were carried out for at least 10 rotations (based on the starting spin period), or until equilibrium was reached (i.e., the point beyond which no further significant change to the largest remnant seemed likely, based on examination of animations of each simulation).

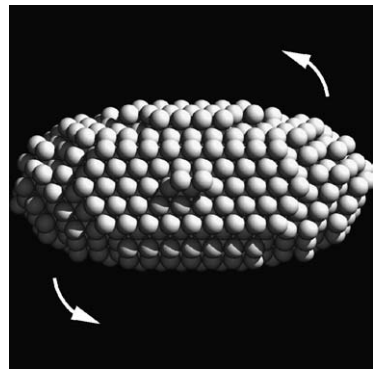

Fig. 1. Sample rubble pile used for testing. This example has 897 particles (the target was 1000), with $q_2 = 0.50$ and $q_3 = 0.48$ (the target was $q_2 = q_3 = 0.5$). The arrows indicate the sense of rotation, in this case around the maximum moment axis.

In order to test the effect of the (normal) coefficient of restitution ϵ_n on the outcome, values of $\epsilon_n = 0.8$ for both the $N \sim 100$ case and $N \sim 1000$ case, and 0.5 for just the $N \sim 100$ case, were investigated, where ϵ_n values of 0 and 1 refer to perfectly inelastic and perfectly elastic outcomes, respectively. The tangential coefficient of restitution ϵ_t was set to unity in all cases, meaning there was no sliding friction between spheres.

Simulations of densely packed self-gravitating particles can be computationally expensive when $\epsilon_n < 1$ if there is no energy gain to offset collisional loss, since the time between collisions can become arbitrarily short. To counteract this, particles colliding at $< 10\%$ of their mutual surface escape speed were forced to have $\epsilon_n = 1$ (cf. the "sliding phase" correction described by Petit and Hénon, 1987), effectively giving the rubble pile a minimum "temperature" that corresponds to a thermal energy much smaller than the gravitational binding energy. However, it is possible for the time between collisions of a pair of particles in a densely packed system to approach zero even at relatively high collision speeds. This phenomenon (called "inelastic collapse" and described in McNamara, 2000; also see McNamara and Young, 1996) was minimized by again setting $\epsilon_n = 1$, thereby halting the collisional cascade, when the code recognized that particles were undergoing tiny but rapid motions between collisions. Occasionally even this technique failed and particles interpenetrated due to roundoff error. In such cases the particles were forced apart again until they were just touching. We found that such incidents were few in number (compared to the typically millions of collisions that were processed per run) and, for the simulations performed here, did not adversely affect the overall outcome.

[7] http://www.cs.wisc.edu/condor/.
[8] http://www.astro.umd.edu/~dcr/Research/borg.html.

Finally, as noted in Leinhardt et al. (2000), neither rolling nor true sliding motions are modeled, and particles cannot remain mutually at rest in contact (i.e., there are no surface normal forces). Instead, the constituent particles of an otherwise quiescent rubble pile are in a constant state of low-energy collisional vibration (dictated by the $\epsilon_n \to 1$ criteria described above). As will be shown, this approximation nonetheless gives the material realistic bulk properties when compared to theoretical granular models.

2.3. Analysis

We distinguish four types of outcome in our simulations of spinning rubble piles: no mass loss or shape change; no mass loss but shape change required; moderate mass loss and therefore shape change; and finally major mass loss with shape change.[9] The largest remaining remnant in each run was determined using the procedure outlined in Leinhardt et al. (2000). For each remnant, the net mass loss (number of particles lost), final shape (axis ratios), and final spin were computed. The latter quantity was determined by first computing the inertia tensor $\mathbf{I}$ of the remnant and the net angular momentum $\mathbf{L}$ of the remnant's constituent particles, relative to the center of mass, and forming $\boldsymbol{\omega} = \mathbf{I}^{-1}\mathbf{L}$ (cf. Richardson, 1995). Results showing initial and final states for each run are presented in Section 3.

2.3.1. Caveats

Precisely measuring the dimensions (and hence bulk density) of a body made up of discrete, finite spheres is challenging because of the bumpiness of the outer surface. For a perfect fluid, or a granular assemblage in the continuum limit, this is not an issue since the outer surface must be smooth in that case. However, in order to compare our results with fluid and continuum limits (Fig. 2a), we must measure the axis ratios of our rubble piles and compute their bulk densities. Our strategy is to solve for the body principal axes as the eigenvectors of the inertia tensor and measure the maximal separation of particles along these axes, taking into account the finite size of the particles. This method ignores any asymmetries, since the center of mass is assumed to coincide with the center of figure, but the cases presented here always satisfied this assumption in any case. However, the ellipsoid described by Eq. (1) for the measured dimensions is generally only an approximation to the actual enclosing shape due to the discrete nature of the spheres, particularly for extreme elongations. For example, a body with a $10:1$ axis ratio ($q_2 = q_3 = 0.1$) could be modeled as a line of 10 identical spheres, but the resulting shape is not well described by an ellipsoid and will lead to imprecision in determining the bulk density. For our purpose we simply assumed an ellipsoid with the measured dimensions was an adequate description of the rubble pile shape in question.

Because of the uncertainties in measuring rubble pile shapes, and moreover the fact that it may not be possible to exactly match a desired axis ratio when generating a rubble pile, the actual initial conditions were not assumed to exactly match the desired initial conditions. This will be evident in the summary plots of the next section, keeping in mind that all bodies were initially as close to being prolate ($q_2 \simeq q_3$) as our numerical resolution would allow. The choice of initial conditions was largely arbitrary anyway; the consequence of the numerical effects described above is that we did not sample parameter space perfectly uniformly. Nonetheless, parameter space coverage was more than adequate for this first investigation.

3. Results and discussion

3.1. Spin tests

Figures 2b–2f summarize the results of the equilibrium spin and shape study. As previously mentioned, Fig. 2a shows certain limiting-case fiducials in the continuum limit that will aid in the interpretation of the numerical results. These fiducials are repeated in Figs. 2b–2f for reference, except that the curves for fluid bodies are shown in cyan (instead of red and green) and only the q_2 curves are shown in Figs. 2c and 2e and the q_3 curves in Figs. 2d and 2f.

Figure 2b uses errorbars to denote the values of q_2 and q_3 for each body as a function of normalized spin $\omega/\sqrt{2\pi G\rho}$ for the $N \sim 1000$, $\epsilon = 0.8$ case. Dark gray errorbars in the background indicate initial conditions while colored errorbars in the foreground indicate final conditions. Since $q_3 \leqslant q_2$ by definition, the measured value of q_3 is represented by the bottom of each errorbar while q_2 is represented by the top. The center of each errorbar is merely the average of q_2 and q_3. Note that obloids have $q_2 \equiv 1$ and proloids have $q_2 \equiv q_3$, so the errorbars give an indication of how far off the bodies are from these ideals. Recall that our intention was to start with perfectly prolate bodies but that resolution effects meant the bodies were only approximately prolate ($q_2 \simeq q_3$) and that the bulk density and initial spin were similarly slightly off from their targets (typically by only a few percent). For this reason the gray errorbars actually have vertical extent in all cases when in fact for proloids they would have no vertical extent. Furthermore, achieving a particular value of q_2 or q_3 was problematic in some cases (e.g., especially $q_2 = 0.9$ or 0.7), as were initial normalized spins > 0.8. As argued in the previous section however, our primary concern is breadth of coverage of parameter space, not uniformity of coverage.

The colored errorbars in Fig. 2b indicate the final configurations of the largest remnant in each simulation. Green indicates bodies that have not suffered any mass loss (i.e., not lost any particles). Yellow indicates remnants that lost up

[9] Note that in his work, Holsapple (2001) did not determine shape change due to plastic flow for his models, but could distinguish between new equilibria and catastrophic disruption on the basis of adopted flow rules.

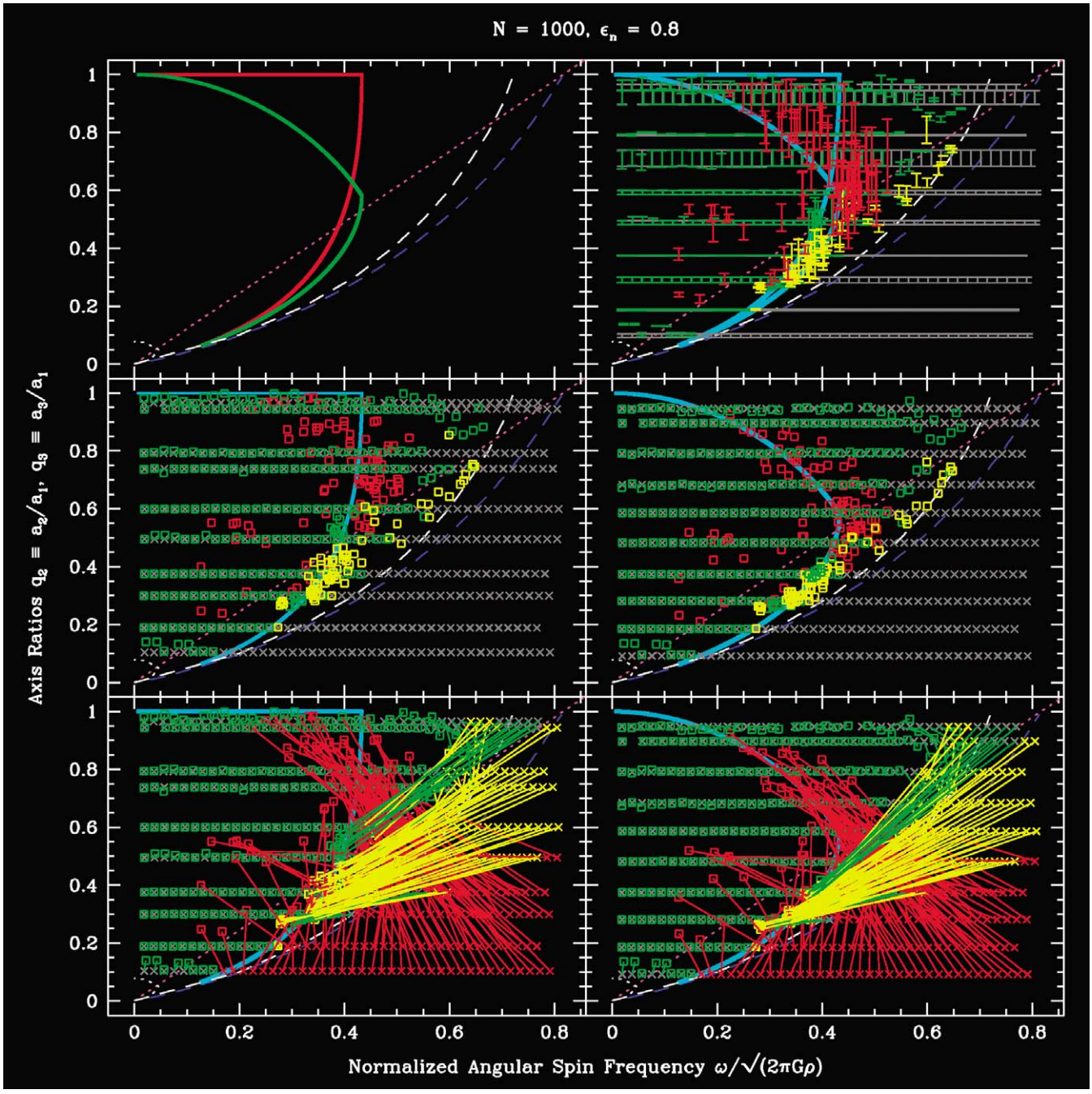

Fig. 2. (Top left, a) Theoretical axis ratio limits for continuum models as a function of normalized angular speed around the maximum moment of inertia. Solid red curve: q_2 for a fluid; solid green curve: q_3 for a fluid (the upper branches of the red and green curves describe the Maclaurin sequence while the lower branches describe the Jacobi sequence); dashed blue curve: Eq. (3), the limiting case for a test particle to remain on the tip of a proloid; dotted magenta line: Eq. (4), the often-used approximation to Eq. (3); dotted/dashed light gray curve: lower/upper limit curve from Holsapple (2001, Fig. 3), for a cohesionless granular proloid with friction angle $\phi = 40°$. (Top right, b) Initial (dark gray) and final (green for no mass loss, yellow for up to 10% mass loss, red for greater than 10% mass loss) configurations for the largest bodies in each simulation, with errorbars indicating q_2 (top) and q_3 (bottom). (Middle left, c) Same as (b) but only for q_2. (Middle right, d) Same as (b) but only for q_3. (Bottom left, e) Same as (c) but with straight lines connecting the initial and final states. (Bottom right, f) Same as (e) for q_3.

to 10% of their initial mass. Typically in such cases mass was shed from the ends of the major axis and the remaining material slumped together to form a smaller body, almost always with a slower normalized rotation. Red indicates remnants that lost more than 10% of their initial mass. Such outcomes were typically catastrophic, leaving a much smaller, rounder, slower-spinning remnant.

Figures 2c and 2d use the same color scheme as Fig. 2b but separate the q_2 data (Fig. 2c) from the q_3 data (Fig. 2d) so trends are easier to distinguish. The initial conditions are shown as small dark gray crosses and the final data points are now represented as open squares. Figures 2e and 2f show the same data but with solid lines now connecting the starting and ending conditions to indicate how bodies have moved in the diagram. The most dramatic cases were usually accompanied by mass loss. For added clarity the initial conditions for cases with mass loss (shown as crosses) use the same color scheme as the final conditions.

Recall that bodies behaving as pure fluids would be expected to lie on the fluid fiducial lines (shown in cyan). The straight dotted line in magenta is the approximate limiting curve from Eq. (4) for a test particle on a rigid proloid. The dashed curved line in blue is Eq. (3) for a test particle on a rigid proloid. Also shown in light gray are the upper and lower limiting curves from Holsapple (2001) for granular material with a friction angle of $\phi = 40^\circ$ in a proloid configuration. Our numerical results lie almost exactly within these latter curves, suggesting that our rubble piles behave, at least in the limiting case, like granular material with $\phi = 40^\circ$. We caution however that other angles are probably consistent with the measurement errors (cf. Section 2.3.1, and Section 3.1.2 below). Indeed, Albert et al. (1997) found $\phi \sim 23.4^\circ$ for a monodisperse population of spheres based on laboratory experiment. It may be that the effective ϕ in our simulations depends to some degree on the numerical resolution (number of particles N), an aspect we plan to investigate in future work (Section 4).

3.1.1. *Spin tests: discussion*

Several trends are readily apparent in Figs. 2b–2f. First, most remnants lie in the upper left of the plots, that is, they have both low-to-moderate spin and elongation. In particular, most of the green points (no mass loss) lie to the upper left of the Maclaurin/Jacobi curves, indicating that perfect rubble piles are capable of retaining a range of shapes (from spherical to highly elongated) independent of the spin rate, up to a maximum *beyond* the fluid limit that is roughly defined by the Holsapple curve. This can be understood by noting that in coarse configurations of a few large spheres, in order for a single rubble particle to move toward a lower energy state, it must first overcome the potential barrier imposed by its large neighbors (analogously, this is how cannonball stacking works). Without an extra input of energy this is not possible, so the shape is retained, even at zero spin. Note extreme elongation at zero spin is also possible. For example, a single line of perfectly aligned massive spheres will maintain their alignment in the presence of self-gravity by virtue of perfectly counteraligned mutual normal forces. This is an elementary example of a configuration that is in unstable equilibrium. However, in the continuum limit, Holsapple (2004) finds a maximum elongation ratio for a prolate body at zero spin of about 0.12 (see their Fig. 8). Our results confirm this lower stability limit (e.g., configurations beginning with aspect ratio of 0.1 at zero or small spin fatten to an aspect ratio of 0.12 or so). Conversely, for low elongations, we find that bodies suffer mass loss or shape change at a slightly slower spin than predicted by the Holsapple curve, which may be a result of the finite nature of our model.

A second trend in Figs. 2b–2f is that, when mass loss occurred, the resulting remnants had a tendency to end up close to the fluid/granular limit curves, or rather, to move within the stability bound for a continuum cohesionless solid with no strain energy. This was particularly true for cases with $\lesssim 10\%$ mass loss (shown in yellow) and final $q_2, q_3 \lesssim 0.5$, and for cases with $\gtrsim 10\%$ mass loss (shown in red) and final $q_2, q_3 \gtrsim 0.5$. From Figs. 2e and 2f, the former group typically originated from bodies with low elongation and rapid spin, while the latter group mostly came from bodies with high elongation and rapid spin. Both groups had in common a fast initial spin (and hence kinetic energy), which suggests that upon reaccumulation there was sufficient free energy to drive the remnants toward the lowest energy state available for their angular momentum, in other words, toward the continuum limits. Note that Fig. 2b indicates that many of these bodies are indeed consistent with Maclaurin spheroids or Jacobi ellipsoids (i.e., the errorbars straddle the requisite curves to some degree). Notable exceptions to these trends include bodies that suffered moderate mass loss and ended up with relatively slow spins (red points well to the left of the limit curves) and bodies that suffered minor mass loss and ended up with relatively fast spins (yellow points to the upper right of the plots, near the Holsapple curve). From Figs. 2e and 2f, these appear to be cases where the combination of the initial shape and spin (either high elongation with modest spin in the former case or low elongation with high spin in the latter) was insufficient to allow the vigorous reshaping of the bodies needed to attain the minimum energy state. It turns out that the red points in question include the relatively small number of cases where the mass loss was between 10 and 50% of the starting mass; most red points suffered more than 50% mass loss.

A third trend, from Figs. 2e and 2f, is that fast-spinning bodies with low elongation had a tendency to shed mass from their tips whereas fast-spinning bodies with high elongation had a tendency to disrupt in a manner reminiscent of the tidal disruption of Comet D/Shoemaker–Levy 9 (SL9) at Jupiter (see, e.g., Asphaug and Benz, 1994). Indeed, tidal encounters provide a torque that, under favorable circumstances, causes a body to spin up and possibly gently shed mass or violently disrupt (e.g., Richardson et al., 1998; Scheeres et al., 2000, 2004). However, direct comparison

of tidal encounters with the present study is only valid for cases where the encounter can be treated as an impulse. Slow or deep encounters result in more complicated disruption scenarios for which the planet's gravity causes significant perturbations over an extended interval. Note also that the starting cases that lose mass are unphysical unless the bodies had some cohesion to start with, requiring an impact or some other impulse to break them up, after which any reaccumulated remnants would be rubble piles.

3.1.2. Conservation of angular momentum

Bodies that change shape and/or spin without losing mass (indicated by green lines in Figs. 2e and 2f) must conserve angular momentum. For uniform rotation about the short axis, the angular momentum is (Holsapple, 2004, personal communication; also see Washabaugh and Scheeres, 2002, Eq. (2))

$$h = \frac{3^{2/3} M (\frac{M}{\rho})^{2/3} (1 + q_2^2) \omega_0}{10 \cdot 2^{1/3} \pi^{2/3} (q_2 q_3)^{2/3}}, \tag{5}$$

where M is the mass of the body and ω_0 is the unnormalized angular speed. Therefore, for constant mass and density, conservation of angular momentum requires

$$\eta \equiv \frac{(1 + q_2^2)\omega}{(q_2 q_3)^{2/3}} = \text{constant}, \tag{6}$$

where $\omega \equiv \omega_0 / \sqrt{2\pi G\rho}$ (from here forward it will be assumed that ω is always normalized in this way). Figure 3 shows the final value of η vs. the initial value for the green cases in Fig. 2 that moved at least 0.01 units in the ξ^2 space defined in the following section (this lower limit roughly corresponds to half the distance between tested values of ω, q_2, and q_3, i.e., a noticeable displacement on the plots of Fig. 2). Ideally data shown in Fig. 3 should lie on the diagonal line $\eta_{\text{final}} = \eta_{\text{initial}}$.

There are two distinct clumps of points in Fig. 3, representing two populations of starting configurations that underwent significant shape and/or spin change without losing mass. The central clump corresponds to the group that began with $\omega \sim 0.6$–0.7 and $q_2, q_3 \sim 0.9$–1.0, while the clump to the right, noticeably ($\sim 20\%$) below the diagonal line, began with $\omega \sim 0.5$ and $q_2, q_3 \sim 0.5$. The actual magnitude of the change in angular momentum, checked by explicitly summing over individual particles, averaged 0.09% over *all* simulations shown in Fig. 2 (i.e., including those with mass loss), with a maximum of 3.2%, standard deviation of 0.31%, and median of 0.012%. Hence the fact that some particles lie well off the diagonal line in Fig. 3 appears to be due to the uncertainties in measuring ω, q_2, and q_3 for these rubble piles (cf. Section 2.3.1). By inspection, we have estimated that errors in axis measurement could be as large as one particle radius along each axis. For $N \sim 1000$ this translates to $\sim 10\%$ measurement error. When propagated through to the expression for η, deviations from the diagonal line in Fig. 3 at least as large as 20% are expected (recall that ω is normalized by ρ, so this introduces density uncertainty as well).

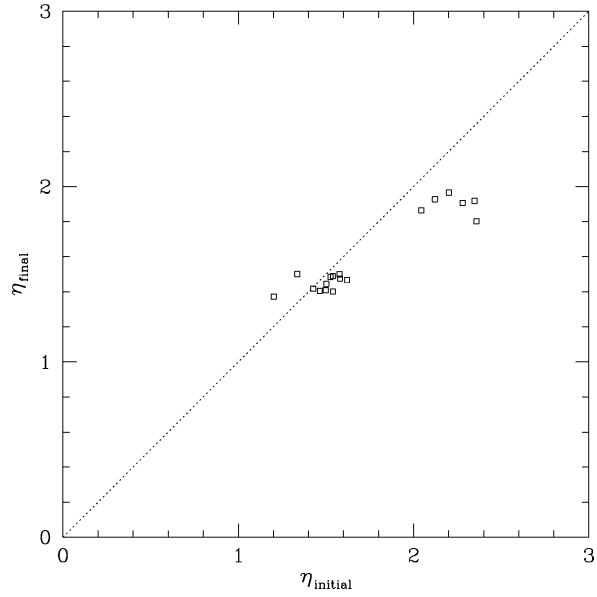

Fig. 3. Initial and final normalized angular momentum as given by Eq. (6) for cases in Fig. 2 that showed significant shape and/or spin change without mass loss. Conservation of angular momentum requires the points to lie on the diagonal line, but uncertainty measuring ω (normalized), q_2, and q_3 for a rubble pile can cause deviations at least as large as those shown here. Angular momentum was actually conserved to better than $\sim 3\%$ in all cases as determined by summing over the individual particles in each simulation.

We conclude that the bodies that suffered no mass loss reshaped themselves along curves of constant angular momentum, within the measurement uncertainties. The fact that there is a systematic deviation from perfect conservation for a particular group may indicate a bias in the measurement uncertainty for those starting conditions. At any rate, internal conservation of angular momentum for each simulation was very good, lending confidence that the dynamics were modeled correctly. Since reaccumulated rubble piles seek the minimum energy state (see previous section), it is likely that bodies that change shape without mass loss are seeking a lower energy state, but cannonball stacking causes them to encounter multiple local minima along the way in which they may get trapped.

3.1.3. Resolution effects

In addition to the $N \sim 1000$, $\epsilon_n = 0.8$ case discussed to this point, we also tested $N \sim 100$ with $\epsilon_n = 0.8$ and with $\epsilon_n = 0.5$. We found no significant difference in outcome between the latter two cases, despite the different restitution coefficients. This is probably because ϵ_n is only important during reaccumulation, when impact speeds are in excess of the sliding limit discussed in Section 2.2, and in such cases repeated collisions would tend to occur. In the limit of many collisions per particle, so long as $\epsilon_n < 1$, the end result is significant dissipation in all cases. Since we evolved all simulations to equilibrium, the fact that there is little difference between the two restitution cases tested is not surprising.

Table 1
Statistical summary of runs

N	ϵ_n	m	%	$\langle\omega_f\rangle$	σ_{ω_f}	max(ω_f)	$\langle e_f\rangle$	σ_{e_f}	max(e_f)	$\sum\xi^2/n_b$
1000	0.8	[0, 1]	100	0.32	0.15	0.66	0.71	0.24	0.99	0.13
1000	0.8	1	61.9	0.27	0.16	0.66	0.69	0.26	0.99	0.10
1000	0.8	[0, 1)	38.1	0.39	0.10	0.65	0.75	0.20	0.98	0.17
1000	0.8	[0.9, 1)	15.8	0.41	0.10	0.65	0.88	0.09	0.98	0.18
1000	0.8	[0, 0.9)	22.3	0.38	0.10	0.52	0.66	0.20	0.97	0.16
1000	0.8	[0.5, 0.9)	7.2	0.35	0.13	0.52	0.74	0.14	0.97	0.14
1000	0.8	[0, 0.5)	15.1	0.40	0.08	0.50	0.61	0.22	0.97	0.17
100	0.8	[0, 1]	100	0.34	0.16	0.67	0.65	0.27	0.97	0.14
100	0.8	1	66.7	0.29	0.17	0.67	0.61	0.30	0.97	0.12
100	0.8	[0, 1)	33.3	0.43	0.09	0.63	0.73	0.17	0.93	0.20
100	0.8	[0.9, 1)	14.9	0.48	0.07	0.63	0.81	0.10	0.93	0.23
100	0.8	[0, 0.9)	18.4	0.40	0.09	0.54	0.67	0.19	0.93	0.17
100	0.8	[0.5, 0.9)	6.0	0.38	0.11	0.51	0.65	0.18	0.89	0.17
100	0.8	[0, 0.5)	12.5	0.41	0.07	0.54	0.68	0.19	0.93	0.18
100	0.5	[0, 1]	100	0.33	0.16	0.67	0.66	0.27	0.97	0.14
100	0.5	1	68.9	0.29	0.17	0.67	0.61	0.30	0.97	0.12
100	0.5	[0, 1)	31.1	0.42	0.09	0.63	0.77	0.14	0.95	0.19
100	0.5	[0.9, 1)	13.0	0.47	0.06	0.63	0.82	0.10	0.95	0.22
100	0.5	[0, 0.9)	18.1	0.39	0.10	0.55	0.73	0.15	0.92	0.17
100	0.5	[0.5, 0.9)	6.5	0.37	0.13	0.55	0.73	0.15	0.92	0.16
100	0.5	[0, 0.5)	11.6	0.41	0.07	0.51	0.73	0.16	0.92	0.18

Here N is the requested number of rubble pile particles (the actual number may be slightly less to satisfy the desired shape); ϵ_n is the normal coefficient of restitution; m is the remnant mass range considered when computing the statistics, in units of the starting mass; % is the percentage of final remnants in mass range m; ω is the remnant's final angular speed of rotation in units of $\sqrt{2\pi G\rho}$, where ρ is the bulk density; e is the remnant's final shape eccentricity; and $\sum\xi^2/n_b$ is a measure of the phase space distance between all final configurations and the nearest fluid configurations in m (see text for details), normalized by the number of bodies. Angle brackets indicate averages and the σ's represent standard deviations.

However, there is a noticeable trend between the $N \sim 1000$ and $N \sim 100$ cases. The rationale for these tests was that with fewer particles it was expected that resolution effects would play a greater role. In particular, we might expect that the coarser resolution (i.e., $N \sim 100$) would make it harder for final configurations to reach the fluid limit (in the case of reaccumulation after disruption, for example), in much the same way that it is easier to knock over a stack of many small cannonballs than a stack of fewer larger cannonballs. To see this, we constructed the metric $\xi^2 = \omega^2 + (\frac{q_2+q_3}{2})^2$, which measures the distance in $(\omega, \frac{q_2+q_3}{2})$ phase space between the largest remnants in each simulation and the fluid limit curves (the average in the second coordinate is used as a proxy for the constraint that q_2 and q_3 are not actually independent for fluids). Dividing the data into various remnant mass bins (m) for each N–ϵ_n model, Table 1 shows this statistic summed over the remnants in each bin and normalized by their total number, along with the mean, standard deviation, and maximum final values of the normalized spin (ω) and eccentricity (e; recall $e \equiv \sqrt{1-q_2^2}$) in each bin. Also shown is the percentage of remnants in each mass bin (the column labeled "%"), where the masses are normalized to the total mass of the system (so a remnant mass range of [0, 1] includes 100% of the mass).

From Table 1 it can be seen that there is little significant difference between the two $N \sim 100$ cases, with the possible exception that $\langle e\rangle$ for the three last mass bins of the $\epsilon_n = 0.5$ case appear systematically higher than those for the $\epsilon_n = 0.8$ case, possibly indicating that these cases (for $\epsilon_n = 0.5$) "froze out" earlier by virtue of the enhanced dissipation; however, the trend is well within the standard deviations of the measurements. On the other hand, both $N \sim 100$ cases tend to have systematically higher mean and maximum spin and lower mean and maximum elongation than the $N \sim 1000$ case for the majority of mass bins, as might be expected if the coarser ($N \sim 100$) piles are more resistant overall to reshaping, by the cannonball stacking argument given earlier. This trend, though weak, seems to be borne out by examining plots analogous to Fig. 2 for the $N \sim 100$ cases (not shown). Finally, the ξ^2 statistic is uniformly lower in *all* mass bins for the $N \sim 1000$ case compared to the other models, showing that on average higher resolution gives rise to more remnants near the fluid limit. However, the interpretation of these results is complicated by the fact that lower resolution remnants have larger axis length measurement uncertainties. A better approach would be to test configurations with resolution significantly *higher* than the $N \sim 1000$ cases, rather than lower, but this is currently computationally prohibitive.

3.2. Case study: Amalthea

A separate investigation we conducted offers more insight into resolution effects on rubble pile dynamics. In 2002, the Galileo spacecraft obtained a bulk density measurement of $850 \pm 200\,\mathrm{kg\,m^{-3}}$ for Amalthea (Anderson et al., 2002; NASA JPL Solar System Dynamics web-

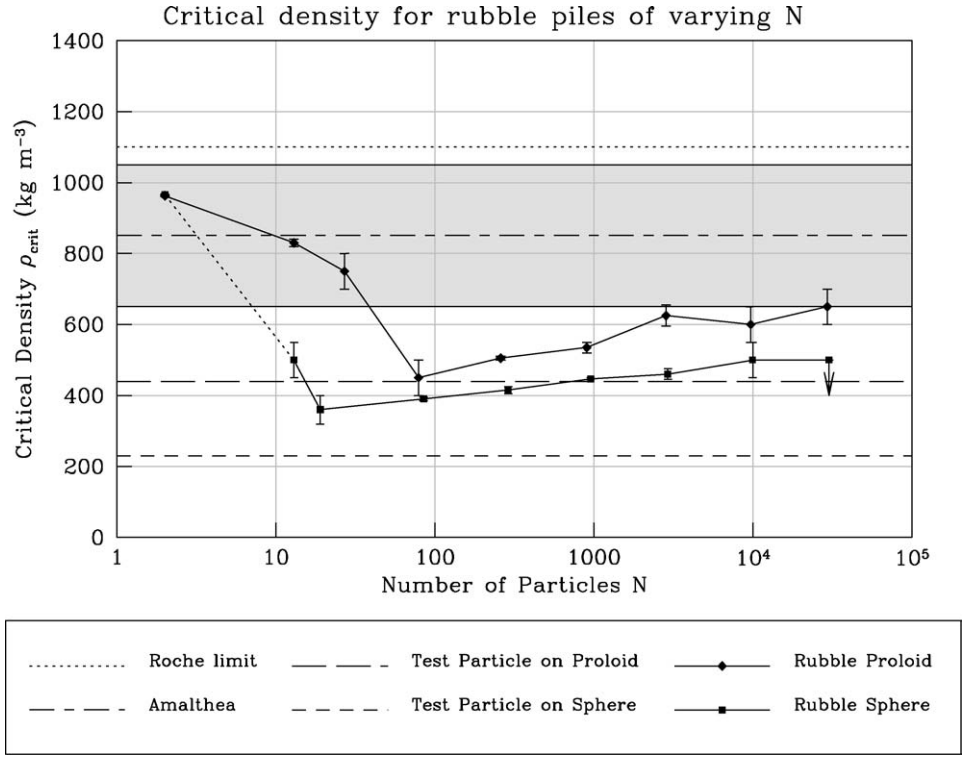

Fig. 4. Critical bulk densities for various configurations located at Amalthea's orbit around Jupiter. The top dotted line indicates the Roche limit (a bulk density of at least this value is required for a perfect fluid to remain stable). The long-and-short-dashed line is the best measured value of Amalthea's density, with the gray region indicating the 1-σ uncertainty in the measurement. The long-dashed line is the limit for a test particle on a 2 : 1-axis-ratio, synchronously rotating proloid. The bottom short-dashed line is the limit for a test particle on a sphere. The filled diamonds show the measured limits for prolate rubble piles of increasing N. The filled squares show the same for a spherical rubble pile. The squares and diamonds are connected by solid lines to aid the eye (the first segment for the spherical pile is dotted to represent the fact that a sphere made up of 2 particles does not really resemble a sphere).

site[10]), a ~ 160 km moon located $\sim 1.8 \times 10^5$ km from Jupiter. Previous to the encounter it was largely assumed Amalthea would have a density perhaps comparable to Io (~ 3500 kg m^{-3}). Amalthea's anomalously low density led it to be characterized as a "rubble pile" (Anderson et al., 2002), although it is also possible the moon instead has tensile strength with large microporosity. We consider the rubble pile model here.

The classical Roche limit for an infinitesimal, homogeneous fluid body of Amalthea's mean density to maintain an equipotential surface in a circular orbit around Jupiter is $\sim 2 \times 10^5$ km (Roche, 1847; also see Lang, 1986, Eq. (3-246); Jupiter parameters from JPL website above), which is *outside* Amalthea's present orbit. Within the measurement uncertainties, this suggests, if Amalthea really is a rubble pile, that its constituent fragments may be sufficiently coarse that they do not behave collectively as a fluid in their present configuration. To test this idea, we conducted a series of simulations using spherical and prolate rubble piles (Amalthea has a $\sim 2 : 1$ axis ratio) to determine whether we could rule out certain configurations for Amalthea (with the usual caveats that we are only simulating idealized rubble piles).

[10] http://ssd.jpl.nasa.gov/.

Figure 4 summarizes the results of this study in a plot of model resolution (number of particles N) vs. critical bulk density (minimum ρ to resist disruption). The figure shows the best estimate of Amalthea's density (gray region centered around 850 kg m^{-3}), with fiducials at 1100 kg m^{-3} (the critical density for a Roche fluid at Amalthea's present distance from Jupiter), 230 kg m^{-3} (the limiting density for a test particle to remain on the surface of a synchronously rotating rigid sphere at Amalthea's mean distance from Jupiter), and 440 kg m^{-3} (the corresponding limiting density for a test particle on the tip of a 2 : 1-axis-ratio proloid with long axis pointing toward Jupiter). The latter two values were obtained by adding the first-order tidal term $-2GM_J/r_A^3$ to the right-hand side of Eq. (A.3) in Appendix A, where M_J is the mass of Jupiter and r_A is Amalthea's mean distance, and setting $q_2 \to 1$ and $q_2 = 0.5$, respectively. We examined models with N varying between 2 and $\sim 3 \times 10^4$. The proloids had the same axis ratios as measured for Amalthea, within numerical limitations (cf. Section 2.3.1). All bodies were synchronously rotating, with longest axis (for the proloids) pointing toward Jupiter, as is the case for Amalthea today. For each model, the bulk density was varied in increments as small as 5 kg m^{-3} in some cases until breakup occurred; these points are shown on the plot with errorbars corresponding to the transition between onset of tidal distur-

bance (reshaping without mass loss) to complete disruption. Cases with large N are less well sampled due to the computational expense of those models. For $N \sim 3 \times 10^4$, only a rough upper limit to the critical density for the spherical case was established.

It can be seen from Fig. 4 that as N increases, both the spherical and prolate cases initially become more resistant to disruption but then gradually become less resistant. This transition can be understood by noting that it is twice as easy to separate two equal-size spheres from each other using tides (the $N = 2$ case; note that the "spherical" model in this case is identical to the prolate model) than it is to remove an infinitesimal test particle from the surface of a single sphere using tides, *for the same total mass and bulk diameter*. As N grows, the model starts to approach the test particle case, in the sense that a single particle on the periphery becomes small compared to the overall size of the body, yet the constituent particles are still large enough to not behave like a granular continuum at equilibrium, owing to cannonball stacking. Eventually however, N becomes large enough that individual particles no longer present a significant potential barrier, so the body can react more easily to the tidal torquing and start to flow. Evidently larger N than we were able to achieve is needed to determine the critical density at which this trend saturates, though other limitations of the numerical model may cause the upwardly rising curves to flatten out prematurely.

Within the 1-σ uncertainties of Amalthea's bulk density it is evident that none of the configurations we tested can actually be ruled out. Only the theoretical fluid configuration exceeds the 1-σ range, but only just barely. However, we note that the two-particle configuration (in which Amalthea would consist of two giant blocks presumably with a common regolith envelope) nonetheless has a higher critical density than the mean measured density of Amalthea. Conversely, configurations consisting of tens to hundreds of solid components have the lowest critical density. We might therefore speculate that Amalthea has the highest probability of being a shattered body that is largely composed of hundreds of competent fragments. But we cannot exclude finer granular configurations, or the possibility that Amalthea is microporous with tensile strength. Regardless, we have demonstrated that perfect rubble piles vary in their response to tidal stress depending on the number of particles and that, given accurate measurements of bulk density, the resulting limits from simulations have promise to place some constraints on the internal configurations of real bodies.

4. Conclusions

We have carried out simulations investigating the spin and shape limits of initially prolate, perfect rubble piles. We find that: (1) unlike perfect fluids, rubble piles can maintain a range of shapes even at zero spin, due to the reshaping barrier presented by individual particles (cannonball stacking); (2) for the same reason, rubble piles can spin faster than a perfect fluid without losing mass, up to a limit in our case that appears to be well represented by the Holsapple (2001) limit for granular material in a prolate configuration with a friction angle of 40°; (3) reaccumulating rubble piles tend toward the fluid/granular limits; and (4) coarse configurations of a few large particles are more resistant to reshaping than fine configurations of many small particles.

The implications of this study are that: (1) numerical rubble piles appear to behave in a manner consistent with theoretical expectations for real granular material, lending support to their validity as analogs for real bodies, though we caution that this only applies to the yield limits (the point at which material starts to flow); and (2) observing the shapes and spins of small bodies in the Solar System can place limits on their possible internal configurations. We also confirm Holsapple's (2001) assertion that asteroid shapes and spins are consistent with rubblized and/or granular configurations. Further, only a tiny amount of strength would be required for a body to survive beyond the limits shown in Fig. 2; thus bodies found in that region cannot be assumed to be "monolithic." One possibility is that geometrical interlocking between (necessarily non-spherical) fragments could be providing strength in these cases, a notion that we will investigate in future work (see below).

It is important to note that most asteroid configurations are inconsistent with fluid shapes (e.g., Pravec et al., 2002; Washabaugh and Scheeres, 2002), which might seem to suggest asteroids are less likely to be *reaccumulated* rubble piles. However, in their lifetime, asteroids undergo many non-disruptive but nonetheless energetic collisions that can alter their spin states and shapes (Asphaug et al., 1998; Paolicchi et al., 2002), moving the bodies further away from the fluid curves. In addition, the YORP thermal effect (Bottke et al., 2002)[11] can dramatically alter spin states over an asteroid's lifetime, at least for those bodies with diameters below a few tens of kilometers. Indeed, YORP has been invoked as a possible formation mechanism for asteroid binaries via mass shedding as the spin rate exceeds the critical threshold (Bottke et al., 2002). Although we did not explicitly search for binaries in our simulations, the fact that many outcomes are qualitatively similar to tidal disruption, and that such events can lead to binary formation (Richardson and Scheeres, 2002; Walsh and Richardson, 2004), suggests this is a plausible mechanism. With large, bulky, interlocking components, or a little bit of cohesion between smaller components, a slowly spun-up fragmented body could avoid mass shedding (which would cause it to restabilize as it loses angular momentum) until the body has made it some dis-

[11] The Yarkovsky–O'Keefe–Radzievskii–Paddack or YORP effect is caused by anisotropic re-radiation of thermal energy following solar heating of a non-spherical body, resulting in a net torque on the body relative to its spin axis.

tance past the cohesionless breakup limit, whereupon it may catastrophically disrupt (Weissman et al., 2003).

The present study was intended to assess the relationship between numerical idealized rubble piles and fluids/granular media. We have made a first step toward that goal. Future studies could investigate a greater range of starting shapes (e.g., obloids or simply random triaxial shapes) and spin orientations (the present study was restricted to spin around the largest inertia moment), use higher resolution (more particles), search for binary formation following mass shedding, look for asymmetric final shapes (we assumed triaxial symmetry), and explore the effect of surface friction (we did not include this in our models). Perhaps of even greater interest however is to move away from idealized monodisperse spherical particles to a range of particle sizes (which can affect the bulk density via drainage of small particles through the cracks between large particles) and ultimately to a range of particle shapes. One approach to the latter goal is to implement composite shapes consisting of spheres fused together, such as dumbbells, cubes, pyramids, etc., which would require solving the Euler equations of rigid body motion with torques (see, e.g., Richardson, 1995), but which would allow the simpler methods of collision detection between spheres to be retained. This facility has been incorporated into `pkdgrav` and testing is currently underway.

Acknowledgments

This material is based upon work supported by the National Aeronautics and Space Administration under Grant No. NAG511722 issued through the Office of Space Science and by the National Science Foundation under Grant No. AST0307549. D.C.R. thanks S. Tremaine and K. Holsapple for motivating this work. R.S. thanks D. Hamilton for guidance. The authors thank W. Bottke, D. Hamilton, K. Holsapple, Z. Leinhardt, P. Michel, M. Miller, and D. Scheeres for helpful comments and advice. The simulations presented in this paper were carried out using the Beowulf cluster administered by the Center for Theory and Computation of the Department of Astronomy at the University of Maryland. Raytracing for Fig. 1 was performed using the Persistence of Vision Raytracer.[12]

Appendix A. Spin limit for a particle on a rigid proloid

A test particle at the tip of a rigid proloid of dimensions $a_3 = a_2 < a_1$ (so $q_3 = q_2 < 1$), rotating with angular frequency ω (unnormalized for this derivation), will barely remain at rest if the gravitational acceleration on the particle is just balanced by the apparent outward acceleration due to the rotation. For an ellipsoid of uniform mass density ρ, the mass element $dm = \rho\, dV$, so the gravitational acceleration is $\iiint_V G\rho\, dV\, \mathbf{s}/|\mathbf{s}|^3$, where G is the gravitation constant and $\mathbf{s}$ is a vector pointing between the mass element and the test particle (see Danby, 1992, Section 5.5, for an alternative approach; also Harris, 2002, Appendix). Expressing the triple integral in cylindrical coordinates (r, ϕ, z), with the particle located at $z = +a_1$, the equilibrium condition may be written as

$$\omega_{\max}^2 a_1 = G\rho \int_{-a_1}^{a_1} \int_0^{a_2\sqrt{1-z^2/a_1^2}} \int_0^{2\pi} \frac{r(z-a_1)}{[(z-a_1)^2 + r^2]^{3/2}} \times d\phi\, dr\, dz, \tag{A.1}$$

where we have exploited the symmetry of the ellipsoid, centered at the origin with the long axis directed along the z-axis, and taken just the magnitude of the net acceleration (it would be directed toward the center of the ellipsoid).

The integrals over ϕ and r are straightforward, leaving

$$\omega_{\max}^2 a_1 = 2\pi G\rho \times \left[2a_1 - \int_{-a_1}^{a_1} \frac{(z-a_1)\, dz}{\sqrt{(z-a_1)^2 + a_2^2(1 - z^2/a_1^2)}} \right]. \tag{A.2}$$

Setting $a_2 = q_2 a_1$, we obtain (using *Mathematica*[13])

$$\omega_{\max}^2 a_1 = -2\pi G\rho a_1 q_2^2 \times \frac{2\sqrt{1-q_2^2} + \ln\left(-\frac{-2+q_2^2+2\sqrt{1-q_2^2}}{q_2^2}\right)}{(1-q_2^2)^{3/2}}. \tag{A.3}$$

Defining the eccentricity $e \equiv \sqrt{1-q_2^2}$ and simplifying, we obtain Eq. (3).

References

Albert, R., Albert, I., Hornbaker, D., Schiffer, P., Barabási, A.-L., 1997. Maximum angle of stability in wet and dry spherical granular media. Phys. Rev. E 56, 6271–6274.

Anderson, J.D., Anabtawi, A., Jacobson, R.A., Johnson, T.V., Lau, E.L., Moore, W.B., Schubert, G., Taylor, A.H., Thomas, P.C., Weinwurm, G., 2002. Gravity field, topography, and interior structure of Amalthea. In: Fall 2002 AGU, P12C-13, pp. 3–4.

Asphaug, E., Benz, W., 1994. Density of Comet Shoemaker–Levy 9 deduced by modelling breakup of the parent "rubble pile." Nature 370, 120–124.

Asphaug, E., Ostro, S.J., Hudson, R.S., Scheeres, D.J., Benz, W., 1998. Disruption of kilometre-sized asteroids by energetic collisions. Nature 393, 437–440.

Binney, J., Tremaine, S., 1987. Galactic Dynamics. Princeton Univ. Press, Princeton. pp. 257–262.

[12] http://www.povray.org/.

[13] http://www.wolfram.com/.

Bottke Jr., W.F., Richardson, D.C., Michel, P., Love, S.G., 1999. 1620 Geographos and 433 Eros: shaped by planetary tides? Astron. J. 177, 1921–1928.

Bottke Jr., W.F., Vokrouhlický, D., Rubincam, D.P., Brož, M., 2002. The effect of Yarkovsky thermal forces on the dynamical evolution of asteroids and meteoroids. In: Bottke Jr., W.F., Cellino, A., Paolicchi, P., Binzel, R.P. (Eds.), Asteroids III. Univ. of Arizona Press, Tucson, pp. 395–408.

Danby, J.M.A., 1992. Fundamentals of Celestial Mechanics, second ed. Willmann–Bell, Richmond, VA. pp. 102–111.

Durda, D.D., Bottke Jr., W.F, Enke, B.L., Merline, W.J., Asphaug, E., Richardson, D.C., Leinhardt, Z.M., 2004. The formation of asteroid satellites in large impacts: results from numerical simulations. Icarus 167, 382–396. Also see Erratum: Icarus 170 (2004) 242, and reprinted article: Icarus 170 (2004) 243–257.

Farinella, P., Paolicchi, P., Tedesco, E.F., Zappalà, V., 1981. Triaxial equilibrium ellipsoids among the asteroids? Icarus 46, 114–123.

Harris, A.W., 1996. The rotation rates of very small asteroids: evidence for "rubble pile" structure. In: Proc. Lunar Planet. Sci. Conf. 27th, pp. 493–494.

Harris, A.W., 2002. On the slow rotation of asteroids. Icarus 156, 184–190.

Holsapple, K.A., 2001. Equilibrium configurations of solid cohesionless bodies. Icarus 154, 432–448.

Holsapple, K.A., 2003. Could fast rotator asteroids be rubble piles? In: Proc. Lunar Planet. Sci. Conf. 34th, p. 1792.

Holsapple, K.A., 2004. Equilibrium figures of spinning bodies with self-gravity. Icarus 172, 272–303.

Hornbaker, D.J., Albert, R., Albert, I., Barabási, A.-L., Schiffer, P., 1997. What keeps sandcastles standing? Nature 387, 765.

Korycansky, D.G., 2004. Orbital dynamics for rigid bodies. Astrophys. Space Sci. 291, 57–74.

Lang, K.R., 1986. Astrophysical Formulae, second ed. Springer-Verlag, Berlin. 280 p.

Leinhardt, Z.M., Richardson, D.C., 2002. N-body simulations of planetesimal evolution: effect of varying impactor mass ratio. Icarus 159, 306–313.

Leinhardt, Z.M., Richardson, D.C., Quinn, T., 2000. Direct N-body simulations of rubble pile collisions. Icarus 146, 133–151.

McNamara, S., 2000. Inelastic collapse. In: Karkheck, J. (Ed.), Dynamics: Models and Kinetic Theory for Non-equilibrium Many Body Systems. Kluwer, Dordrecht, pp. 267–277.

McNamara, S., Young, W.R., 1996. Dynamics of a freely evolving, two-dimensional granular medium. Phys. Rev. E 53, 5089–5100.

Michel, P., Benz, W., Richardson, D.C., 2004. Catastrophic disruption of asteroids and family formation: a review of numerical simulations. Planet. Space Sci. In press.

Paolicchi, P., Burns, J.A., Weidenschilling, S.J., 2002. Side effects of collisions: spin rate changes, tumbling rotation states, and binary asteroids. In: Bottke Jr., W.F., Cellino, A., Paolicchi, P., Binzel, R.P. (Eds.), Asteroids III. Univ. of Arizona Press, Tucson, pp. 517–526.

Petit, J.-M., Hénon, M., 1987. A numerical simulation of planetary rings. I. Binary encounters. Astron. Astrophys. 173, 389–404.

Porco, C.C., Throop, H.B., Richardson, D.C., 2003. Saturn's particle disk and the A ring azimuthal asymmetry. Bull. Am. Astron. Soc. 35, 929. Abstract.

Pravec, P., Harris, A.W., 2000. Fast and slow rotation of asteroids. Icarus 148, 12–20.

Pravec, P., Harris, A.W., Michalowski, T., 2002. Asteroid rotations. In: Bottke Jr., W.F., Cellino, A., Paolicchi, P., Binzel, R.P. (Eds.), Asteroids III. Univ. of Arizona Press, Tucson, pp. 113–122.

Richardson, D.C., 1995. A self-consistent numerical treatment of fractal aggregate dynamics. Icarus 115, 320–335.

Richardson, D.C., Scheeres, D.J., 2002. Asteroid satellites formed by tidal disruption. ESA SP, vol. 500. pp. 737–739.

Richardson, D.C., Bottke Jr., W.F., Love, S.G., 1998. Tidal distortion and disruption of Earth-crossing asteroids. Icarus 134, 47–76.

Richardson, D.C., Quinn, T., Stadel, J., Lake, G., 2000. Direct large-scale N-body simulations of planetesimal dynamics. Icarus 143, 45–59.

Richardson, D.C., Leinhardt, Z.M., Melosh, H.J., Bottke Jr., W.F., Asphaug, E., 2002. Gravitational aggregates: evidence and evolution. In: Bottke Jr., W.F., Cellino, A., Paolicchi, P., Binzel, R.P. (Eds.), Asteroids III. Univ. of Arizona Press, Tucson, pp. 501–515.

Roche, M.E., 1847. Mémoire sur la figure d'une masse fluide (soumise à l'attraction d'un point éloingé). Acad. Sci. Montpellier 1, 243–262, 333–348.

Roig, F., Duffard, R., Penteado, P., Lazzaro, D., Kodama, T., 2003. Interacting ellipsoids: a minimal model for the dynamics of rubble-pile bodies. Icarus 165, 355–370.

Scheeres, D.J., Ostro, S.J., Werner, R.A., Asphaug, E., Hudson, R.S., 2000. Effects of gravitational interactions on asteroid spin states. Icarus 147, 106–118.

Scheeres, D.J., Marzari, F., Rossi, A., 2004. Evolution of NEO rotation rates due to close encounters with Earth and Venus. Icarus 170, 312–323.

Stadel, J., 2001. Cosmological N-body simulations and their analysis. Thesis. University of Washington, Seattle. 126 p.

Tanga, P., Weidenschilling, S.J., Michel, P., Richardson, D.C., 2004. Gravitational instability and clustering in a disk of planetesimals. Astron. Astrophys. In press.

Walsh, K.J., Richardson, D.C., 2004. Direct N-body simulations of rubble pile collisions in strong tidal fields: applied to Saturn's F ring. Bull. Am. Astron. Soc. 35, 1486. Abstract.

Washabaugh, P.D., Scheeres, D.J., 2002. Energy and stress distributions in ellipsoids. Icarus 159, 314–321.

Weidenschilling, S.J., 1981. How fast can an asteroid spin? Icarus 46, 124–126.

Weissman, P.R., Richardson, D.C., Bottke Jr., W.F., 2003. Random disruption of cometary nuclei by rotational spin-up. Bull. Am. Astron. Soc. 35, 1012. Abstract.